Chapter4

Large Scale Production of Transition Metal Oxides Nano Sheets by Mixed Solvent Exfoliation for Supercapacitor Application

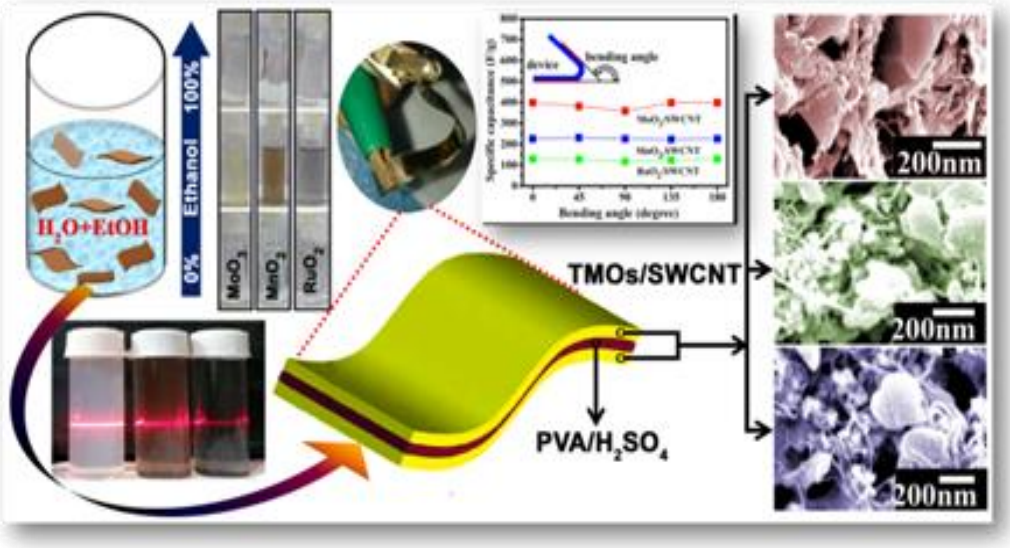

Work presented in this chapter has been published in:

***(1)New J. Chem.*, 2019, 43, 12385-12395**

Shibsankar Dutta, Shreyasi Pal, Sukanta De

(2) *AIP Conf. Proc.*, 2018, 1953, 030145

Shibsankar Dutta, Shreyasi Pal and Sukanta De

4.1. Introduction

This chapter enlightens a simple mixed solvent assisted ultrasonic method to exfoliate transition metal oxides (TMOs) nano sheets using the proper composition of ethanol and water. These well dispersed stable solutions were used to make thin film of TMOs nanosheets which can be readily transferred on wide range of substrates for different applications. TMOs/SWCNT based solid state flexible supercapacitors demonstrated enhanced electrochemical performance.

A number of nanostructured pseudocapacitive materials including transition metal oxides (TMO), [1-9] transition metal dichalcogenides [10], hydroxides[11-13] and conductive polymer materials[14-18] have been used for supercapacitor applications. Among them 2-D graphene analogues (GA) are the best choices for the highly flexible ultrathin-film supercapacitor.[10,11,19] 2-D nanomaterials provides remarkable prospects for both fundamental studies and several technological applications due to their unique and intriguing properties,[20-24] Therefore, the large scale production of 2-D pseudocapacitive materials is much needed for constructing high performance flexible supercapacitors.

In their 2-D structure, inorganic layered materials such as transition metal oxides (MnO_2, RuO_2, MoO_3, TiO_2 etc) and transition metal dichalcogenides (MoS_2, WS_2, VS_2, etc) for their unique properties becomes promising candidates for topological insulators, energy harvesters, thermal conductors, and transistors.[1-9,25-30] Among them transition metal oxides play importance roles to develop environment friendly energy storage devices in the form of pseudocapacitors.[31-34]To exploit their full potential layered materials must be exfoliated. Liquid phase exfoliation of layered materials is most appropriate technique to produce 2-D nanomaterials for many practical applications, especially for thin film formation.[35-41] Depending on the materials, certain solvents [36,38,40-44] or solvent blends,[45] aqueous surfactant solutions,[35,39,46] or polymer solutions[47,48] can be used as stabilizing liquids. For application in supercapacitor electrodes, liquid suspended 2-D nanomaterials or their composite needs to process into films. Liquid phase exfoliated 2-D TMOs and their composites with carbonaceous materials could be suitable to develop thin film flexible electrodes for application in supercapacitors due to excellent electrochemical properties that come from rich selection of atomic types in the 2D lattice plane. Non-volatile high boiling point organic solvents are suitable for liquid

exfoliation according to the thermodynamics study, but non-volatile solvents are difficult to remove after film formation, which provides us the limitations of their use in practical device applications. [39,40,49] Also complete removal of surfactants or polymers from thin films prepared from aqueous surfactant solutions or polymer solutions suspended 2-D nanomaterials is very difficult. The water base mixed solvent is not only suitable to remove easily; they are much less toxic compare to other organic solvents such as NMP, DMF, iso-propanol, chloroform, acetone, DMSO etc. If we can achieve to exfoliate layered transition metal oxides in to their 2-D nanosheets in large scale in water base mix solvents, could be useful to fabricate eco-friendly devices with high performance.

4.2. Experimental section

All the chemicals, Molybdenum Trioxide (MoO_3) (99.5%), Manganese (IV) Oxide (MnO_2) (≥90%), Ruthenium (IV) Oxide (RuO_2) (99.9%) were bought from Sigma-Aldrich. Ethanol and deionized water (D.I.) involved in this work were bought from Merck. Three different transition metal oxides (MoO_3, RuO_2, and MnO_2) were dispersed in different vol% ethanol/water mixture with an initial concentration 20 mg/ml using high power tip sonicator for 30 minutes followed by bath sonicator for 6 hours. Subsequently, they were centrifuged at 1500 rpm for 90 minutes. The supernatants having high concentrations of 2D TMOs flakes were decanted and subjected to further characterization. The Schematic diagram of the mixed solvent exfoliation of the 2-D materials is shown in the fig. 4.1.

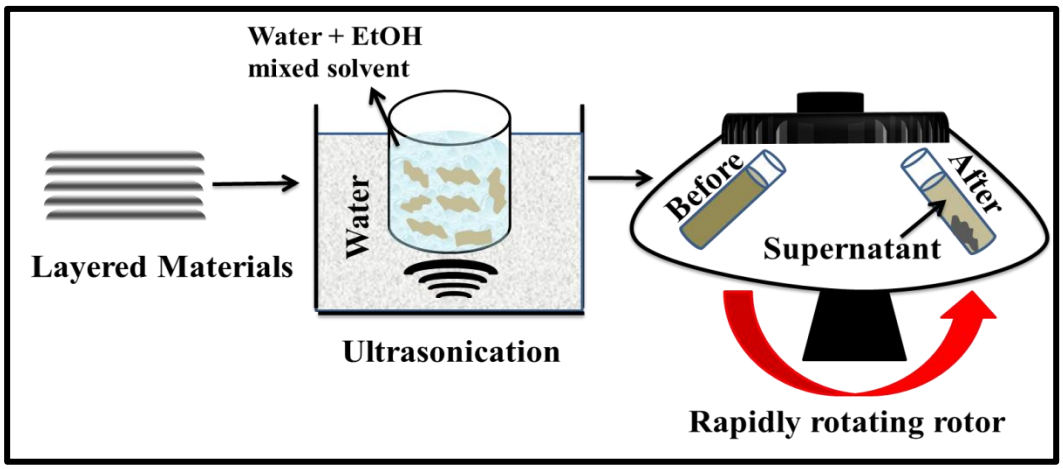

Figure 4.1 Schematic diagram of the mixed solvent exfoliation of the 2-D materials.

4.3. Thin Films Preparation and Device Fabrication

4.3.1. Symmetric flexible supercapacitor fabrication

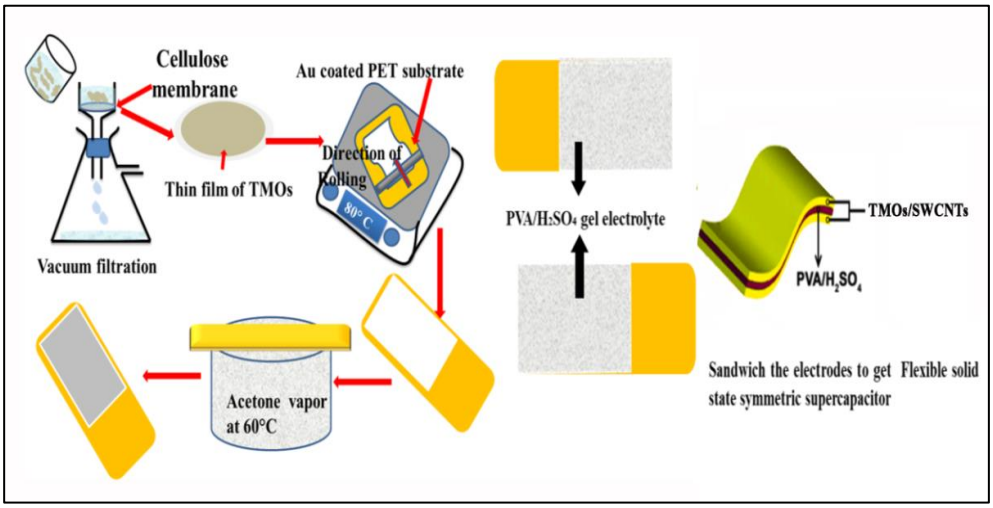

Figure 4.2 Schematic diagrams of Thin Films Preparation and Device Fabrication.

The dispersion of TMOs nanosheets prepared in this method allowed us to make thin films of TMOs nanosheets and their composites with carbonaceous nanostructure by vacuum filtration with thickness ranging from a few nanometers to micrometers. The thin films were then transferred onto a flexible gold coated PET substrate by acetone vapor and acetone bath treatments for device fabrication. Fig.4.2 represents the thin films and device fabrication technique.

4.3.2. In-plane supercapacitor device fabrication

In planner supercapacitors, requirement of a separator is eliminated because the electrolyte ions are transported two-dimensionally. Here we present a mixed solvent exfoliation of MnO_2 nanosheets for high performance planer supercapacitors. In particular, the planar structures supercapacitors constructed by MnO_2 nanosheets integrated with SWCNT. Schematic 4.3 represent the in-plane device fabrication technique.

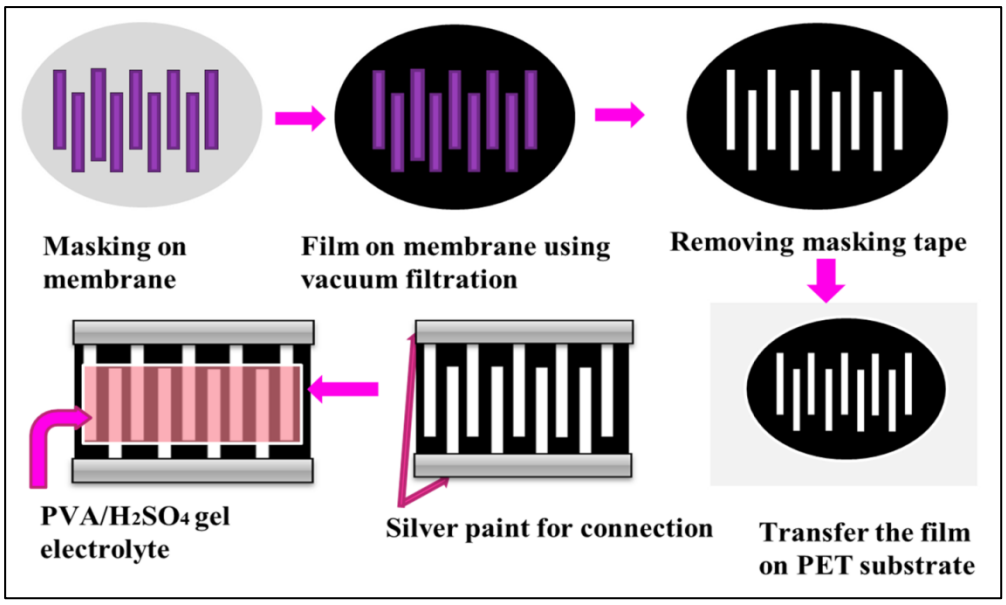

Figure 4.3 Schematic diagrams of In-plane supercapacitor fabrication.

4.4. Materials Characterization

The as-synthesized samples were characterized using UV-Vis spectroscopy (Lambda-950 spectrometer, Perkin Elmer, USA), Raman spectroscopy (IHR550 and the laser of excitation wavelength 532 nm), transmission electron microscope (TEM, JEM-2010), field emission scanning electron microscope (FESEM HITACHI S-4800), atomic force microscopy (VEECO di CP-II AFM), X-ray photoelectron spectroscopy (ULVAC-PHI5000 Versa Probe II spectrometer) with A1 Kα radiation source of photon energy 1486.6 eV. BET analyses of the samples were studied using Autosorb iQ Station 1 instrument using liquid nitrogen at 77 K. All Electrochemical measurements were done using CHI 660E.

4.5. Results and discussion

4.5.1. Exfoliation of TMOs:

To explore the possibilities of liquid phase exfoliation of Transition metal oxides (TMOs) in mixture of two low boiling point and volatile solvents, we have sonicated as received TMOs (MoO_3, MnO_2 and RuO_2) with initial concentration (C_i) 20 mg/ml in mixed solvents of water and ethanol with different volume fractions and centrifuge to get rid of un-exfoliated oxide materials. Digital images of suspensions containing exfoliated MoO_3, MnO_2 and RuO_2 in different ethanol/water mixtures in inset of Figure 4.4 (a-c), shows that the concentration of suspension is varying with ethanol/water ratio. To analyze quantitatively, we have recorded absorption spectra for all dispersions and took the measured of absorbance per unit cell length (A/l) at 375 nm, 380 nm and 450

nm for MoO_3, MnO_2 and RuO_2 respectively which can be used as metric to determine the concentration of TMOs in dispersion. The variation of A/l with volume fraction of ethanol in water (Figure 4.4 (a-c)) clearly shows that pure ethanol or pure water hardly can disperse oxide materials but the concentrations of TMOs dispersions are directly dependent on the volume fraction of ethanol in water with peak at 65% ethanol in water for MoO_3. Whereas for both MnO_2 and RuO_2 peak value of A/l is at 50% mixed solvent.

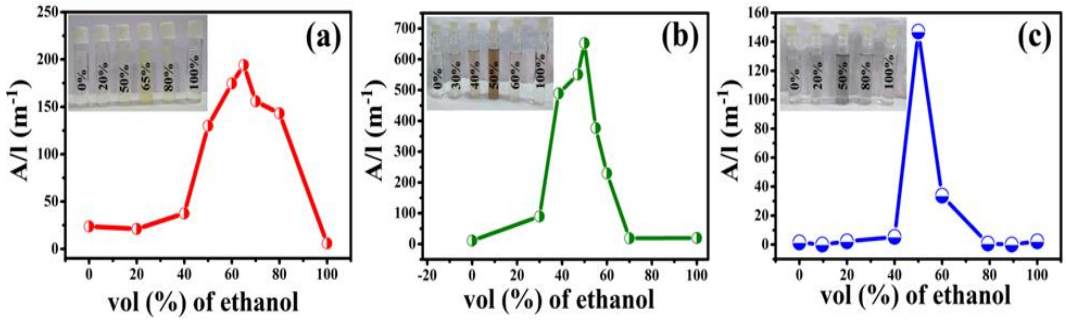

Figure 4.4. (a-c) Graph of A/l vs volume fraction (ethanol) in water for the MoO_3, MnO_2 and RuO_2 nanosheets respectively; Inset showing their corresponding digital images of different vol% EtOH

The dissolution behavior can be explained by the Hansen solubility parameter (HSP) [50-51] theory based on the three solubility parameters, these three dispersive (δ_D), polar (δ_P) and hydrogen bonding (δ_H) solubility parameters of solvent and solute are interrelated by the equation 1.

$$\boldsymbol{R_a = [4(\delta_{Dsolv} - \delta_{Dsolu})^2 + (\delta_{Psolv} - \delta_{Psolu})^2 + (\delta_{Hsolv} - \delta_{Hsolu})^2]^{\frac{1}{2}}} \quad \textbf{(1)}$$

The solubility directly depends on the HSP distance (R_a) value, smaller R_a value provides us higher solubility.

Mixed solvent exfoliation can also be explained by Hansen theory where the each of three parameters is linear function of the volume fraction of the composition [equation 2].

$$\boldsymbol{\delta_{blend} = \sum \emptyset_{n,comp} \delta_{n,comp}} \quad \textbf{(2)}$$

Where ∅ defines the volume fraction of each composition. Based on these two equations different solvent mixture can be predicted for the nanomaterial's exfoliation.

Initially the dispersed concentration can be measured by filtering an appropriate amount of the dispersion and weighing the deposited film. A sample of stock dispersion was then serially diluted with solvent (65% ethanol in water for MoO_3 and 50% ethanol in water for MnO_2 and RuO_2) and measured the absorbance. A straight line fit of absorbance per unit length (A/l) Vs concentration (after centrifuge) as shown in Figure 4.5(a-c), gives the accurate value of absorption coefficient (α). Measured α (at 375 nm) for MoO_3 is 596 mg^{-1} ml m^{-1} and is in reasonable agreement with the previously reported value [41] (note: we have calculated from their reported A/l and concentration value to compare), gives the concentration of dispersed MoO_3 to be 0.33 mg/ml. Most interestingly this is almost 3 times higher than that of in IPA, [41] even the initial concentration was 15 times lower in our case. Absorption coefficient for MnO_2 (at 380 nm) and RuO_2 (at 450 nm) were measured to be 2937 mg^{-1} ml m^{-1} and 641 mg^{-1} ml m^{-1} respectively. The obtained concentration of the dispersed MnO_2 and RuO_2 (C_i=20 mg/ml) was 0.22 mg/ml and 0.23 mg/ml respectively.

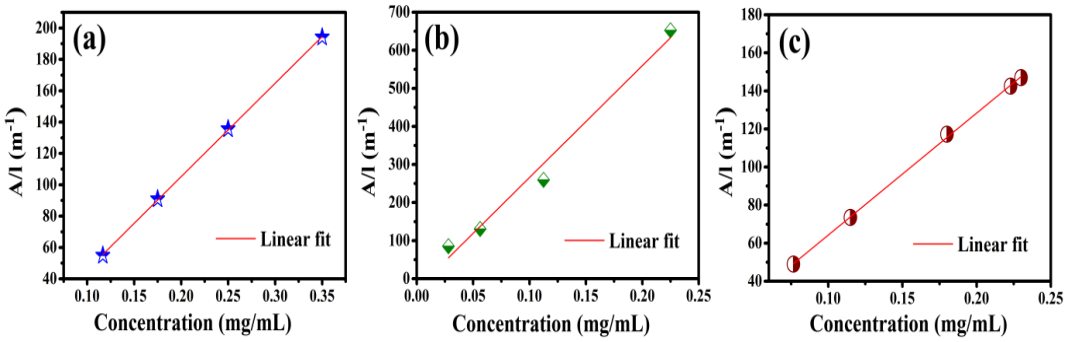

Figure 4.5. Absorbance per unit length (A/l) vs concentration (a) MoO_3, (b) MnO_2, (c) RuO_2.

Maximize the dispersed concentration is very much required for applications and previous report shows that initial concentration plays an important role in it. To address this, with the knowledge of different parameters including the composition of mixed solvents for the stable dispersion we have prepared dispersions for a range of initial concentration (C_i) of oxide materials. We have plotted absorbance per unit length (A/l) vs C_i shown in Figure 4.6(a-c), observing a linear increase in dispersed concentration for all three oxides upto C_i = 60mg/ml after which saturation of solute in solvents is approached.

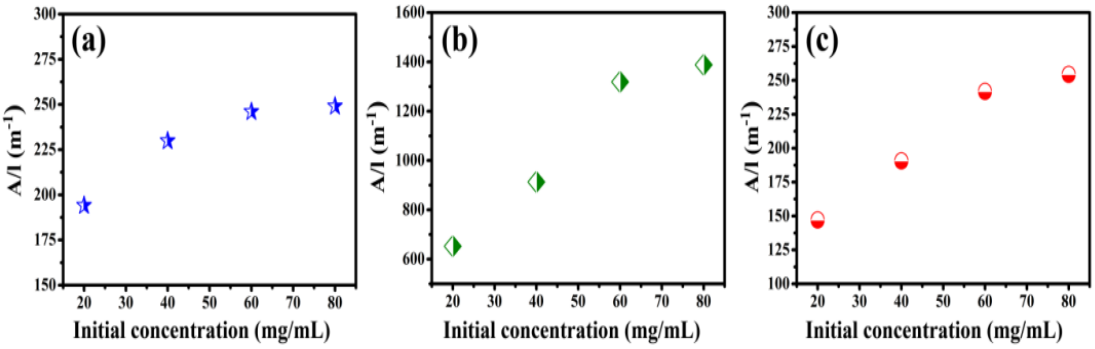

Figure 4.6. Absorbance per unit length (A/l) vs initial concentration (a) MoO_3, (b) MnO_2, (c) RuO_2.

The final concentrations of dispersions were obtained 0.42 mg/ml, 0.47 mg/ml and 0.40 mg/ml for MoO_3, MnO_2 and RuO_2 respectively. The dispersed concentrations of exfoliated TMOs are much higher than the previously reported data's.[41, 52] The TMOs nanosheets were well dispersed in ethanol/water mixed solution showing the Tyndall effect (Figure 4.7).

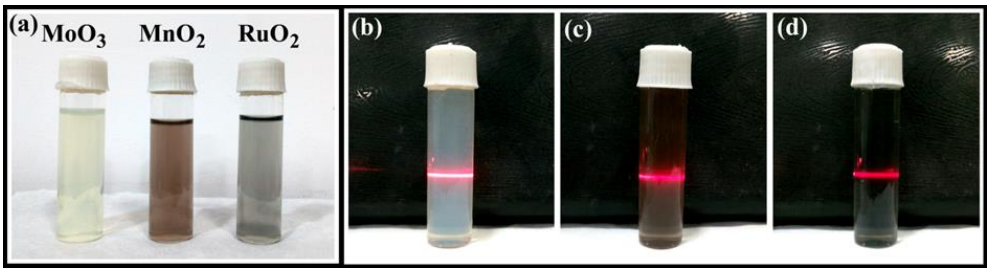

Figure 4.7. (a) Digital images of the MoO_3, MnO_2 and RuO_2 nanosheets dispersion in Ethanol/ water, (b-d) Tyndall effect of the exfoliated MoO_3, MnO_2 and RuO_2 nanosheets respectively.

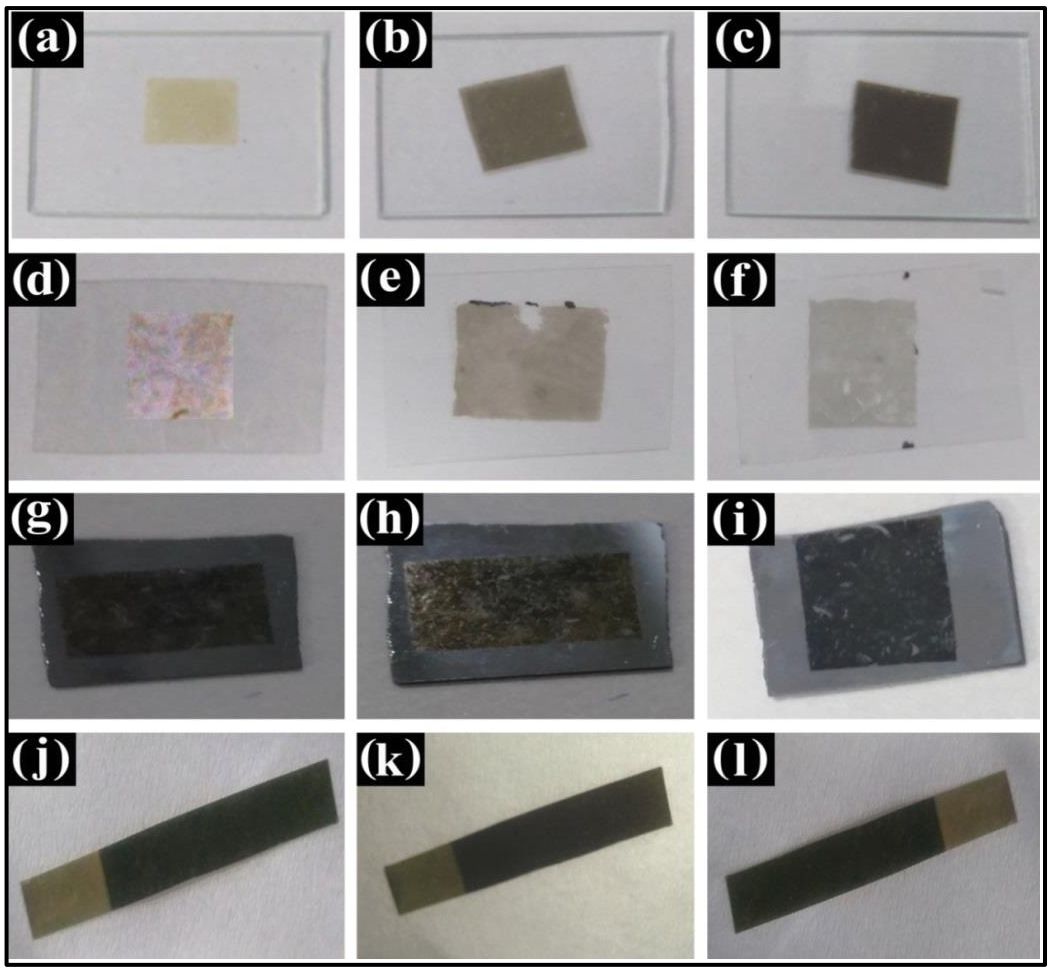

Figure 4.8. MoO_3, MnO_2 and RuO_2 nanosheets thin films on (a-c) glass, (d-f) PET substrate respectively. MoO_3/SWCNT, MnO_2/SWCNT and RuO_2/SWCNT nanocomposites thin films on (g-i) Si substrate and Au coated PET (j-l) substrate respectively

Once we have stable dispersions, thin films of bare TMOs can be prepared by vacuum filtration[41] with thickness ranging from few nanometers to few hundreds of micrometer on cellulose membrane. These thin films can be deposited on suitable substrate as required for device applications. We have shown our films can be transfer on different substrates as shown in the Figure 4.8.

4.5.2 Structural and morphological characterization

The atomic force microscopy (AFM) images shown in Figure 4.9(a-c) of the metal oxides clearly revealed the presence of nanosheets of the metal oxides with an average thickness of 1.85 nm for MoO_3, 1.07 nm for MnO_2 and 2.1 nm for RuO_2 respectively, denoting that our exfoliated metal oxides are mostly bi-layers.[53-55]

For detail structural and morphology study, TEM analysis was performed on exfoliated TMOs by depositing few drops of each dispersion onto TEM grids. In all cases, a large numbers of quasi-2D nanosheets were seen, with typical example as shown in Figure 4.10(a-c). Figure 4.10a represents the TEM image of MoO_3 nanosheet with lateral dimension of ~300 nm to 400 nm. We also studied HRTEM imaging of exfoliated MoO_3, which clearly shows the crystalline structure as displays in the Figure 4.10d. The measured interplanar spacing of MoO_3 nanosheet is 0.39 nm and 0.37 nm, corresponds to the typical interplanar spacing of the (100) and (001) respectively.[56,57] Low magnification TEM image in the Figure 4.10b displays the sheet like morphology of MnO_2 with lateral dimension ~300 nm. High resolution TEM (HRTEM) images of the nanosheets in Figure 4.10e clearly shows that MnO_2 nanosheets were crystallized with the interplanar distance of 0.253 nm corresponding to the (200) plane.[58-60] 2-D nanosheet of RuO_2 have lateral dimension also of ~100 nm measured from TEM image as shown in the Figure 4.10c and lattice spacing of 0.237 nm corresponds to the (110) plane, clearly shown in the HRTEM image displayed in Figure 4.10f.[61-63] Further the SAED patterns of all TMOs (insets of Figure 4.10(d-f)) indicate their single crystalline nature. Lateral dimension of TMOs nanosheets measured from low resolution TEM images are in good agreement with the dimension of nanosheets in AFM images.

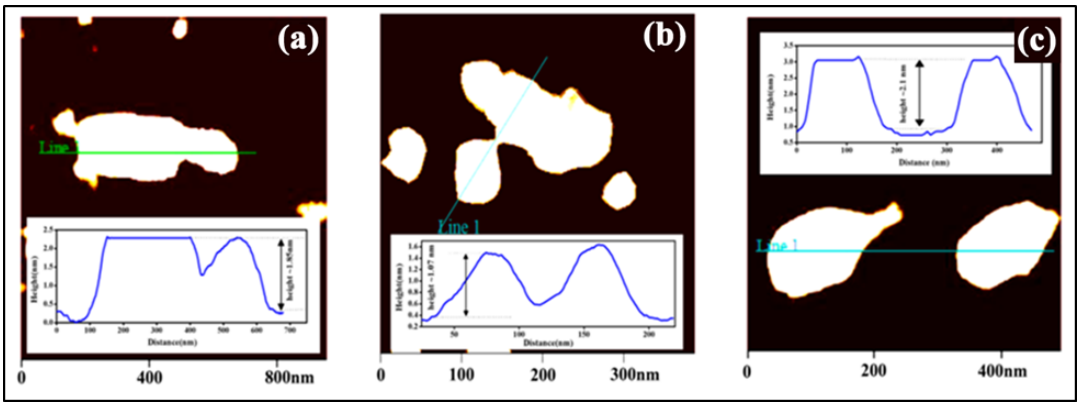

Figure 4.9. Atomic force microscopy (AFM) analysis of (a) MoO_3, (b) MnO_2 and (c) RuO_2 nanosheets respectively

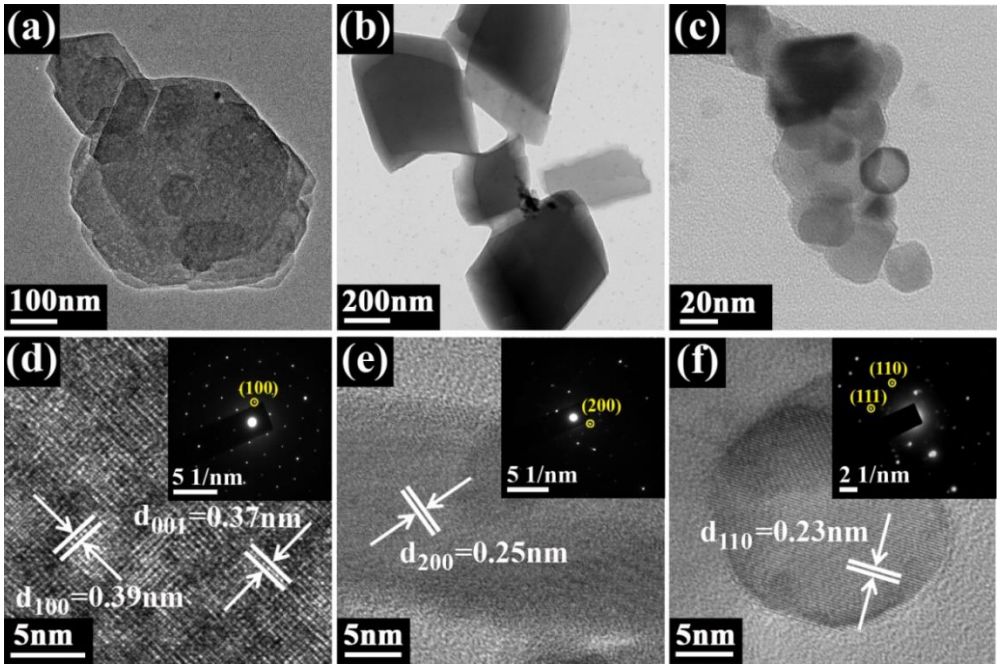

Figure4.10. (a-c) Transmission electron microscopy (TEM) images and (d-f) high-resolution TEM analysis with selected area electron diffraction (SAED) pattern in the inset of MoO_3, MnO_2 and RuO_2 respectively.

Figure 4.11 (a-c) displays the Raman spectra of the exfoliated metal oxide thin films. Three main peaks at 671, 827 and 965 cm^{-1} in the Figure 4.11a were observed for the MoO_3.[53] The 671 cm^{-1} peak is assigned to the stretching mode of triply coordinated oxygen (Mo_3–O) which arises from edge-shared oxygen atoms in common to three octahedral. The peak at 827 cm^{-1} is attributed to the doubly coordinated oxygen (Mo_2–O) stretching mode which results from corner-sharing oxygen atoms common to two octahedral.[64] Finally, the peak at 995 cm^{-1} is assigned to the terminal oxygen (Mo^{6+}=O) stretching mode which results from an unshared oxygen. The Raman spectrum of thin film of exfoliated MnO_2 in Figure 4.11b shows peaks at 510, 575, and 642 cm^{-1}, almost identical as reported previously.[65] The peak at 642 cm^{-1} corresponding to the symmetric stretching vibration ν_2 (Mn–O) of MnO_6 groups. Whereas the band located at 575 cm^{-1} is due to the ν_3 (Mn–O) stretching vibration in the basal plane of [MnO_6] sheets. The three major Raman features located at 528, 644 and 716 cm^{-1} of RuO_2 presented in the Figure 4.11c correspond to E_g, A_{1g} and B_{2g} modes respectively.[66]

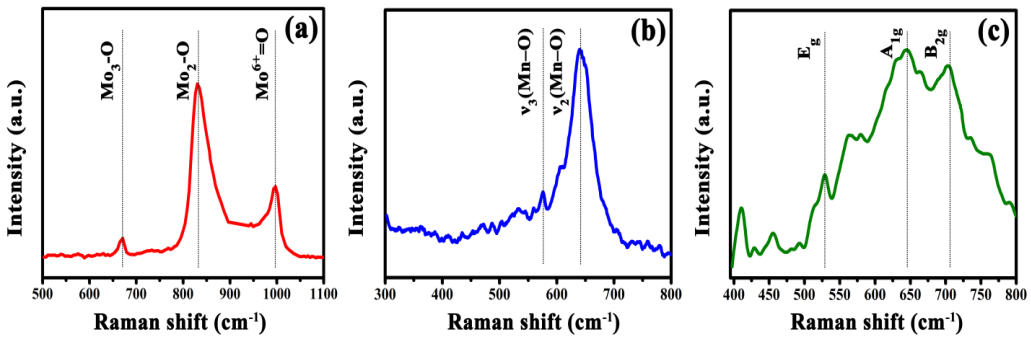

Figure 4.11. Raman Spectra of MoO_3 (a), MnO_2 (b) RuO_2(c) nanosheets thin films on silicon

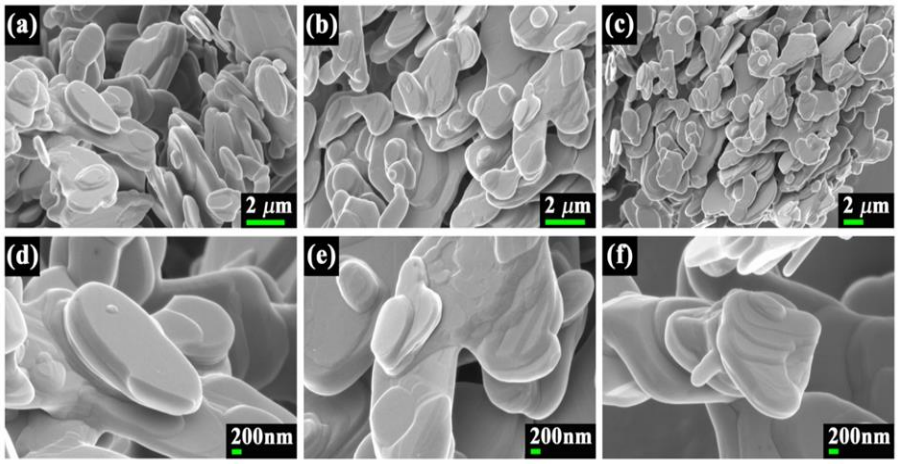

Figure4.12. (a,b,c) FESEM images of the bulk MoO_3, MnO_2, RuO_2; (d,e,f) showing their high magnification FESEM images respectively.

Figure 4.12 shows FESEM images of bulk TMOs, which indicates that bulk TMOs are layered structure. Figure 4.13 (a-c) displays FESEM images of the TMOs nanosheets. 2-D nanosheet of MoO_3 have lateral dimension ~200 nm to 300 nm as shown in the Figure 4.13a, whereas the average lateral dimension of MnO_2 and RuO_2 nanosheets are 250 nm and 100 nm respectively. FESEM was done on the TMOs dispersion after filtering, so it is quite difficult to get actual boundary of the TMOs to determine the flake size individually. TEM was done on exfoliated dispersions of TMOs where we get the actual size of the individual nanosheets as discuss previously. Liquid phase exfoliated stable dispersion facilitate formation of hybrids or composites of 2D nanomaterials with polymers, carbon nanostructures or other different nanomaterials.

After ultrasonic agitation of TMOs and SWCNT might be exfoliated and dispersed in ethanol/water mixer and forming a homogeneous solution of TMOs/SWCNT, which clearly shows in the FESEM images of the TMOs/SWCNT thin films on cellulose membrane [Figure 4.13(d-f)]. The as-prepared composites exhibited an interconnected porous network. In addition, the mesoporosity in the electrode serve as a path, which allow to access of electrolyte to the internal surface of the TMOs.[67]

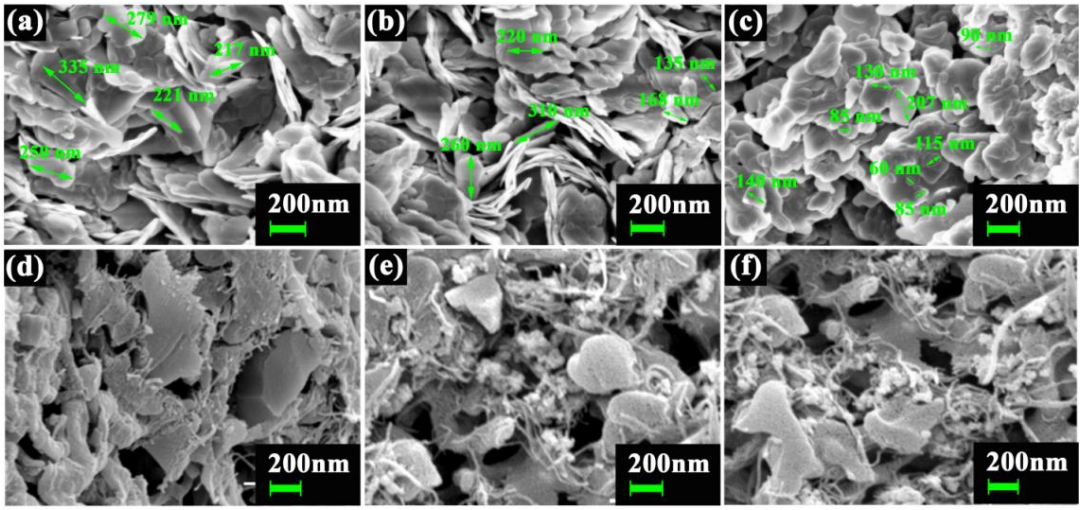

Figure 4.13 FESEM images of (a-c) metal oxide nanosheets (MoO_3, MnO_2, RuO_2) and (d-f) their nanocomposites (MoO_3/SWCNT, MnO_2/SWCNT, RuO_2/SWCNT) respectively.

To investigate the oxidation state of TMOs in the TMOs/SWCNT composites, the samples were further characterized by XPS. Figure 4.14(a,e,i) shows the XPS survey scan of three composites. No additional peak except Mo, O and C (for MoO_3/SWCNT), Mn, O and C (for MnO_2/SWCNT), and Ru, O and C (for RuO_2/SWCNT) was observed from the XPS survey scan. Figure 4.14b shows the Mo 3d spectrum, where two peaks located at 232.5 and 235.6 eV can be attributed to the Mo $3d_{5/2}$ and Mo $3d_{3/2}$ respectively, indicating 6^+ oxidation states for Mo.[68]

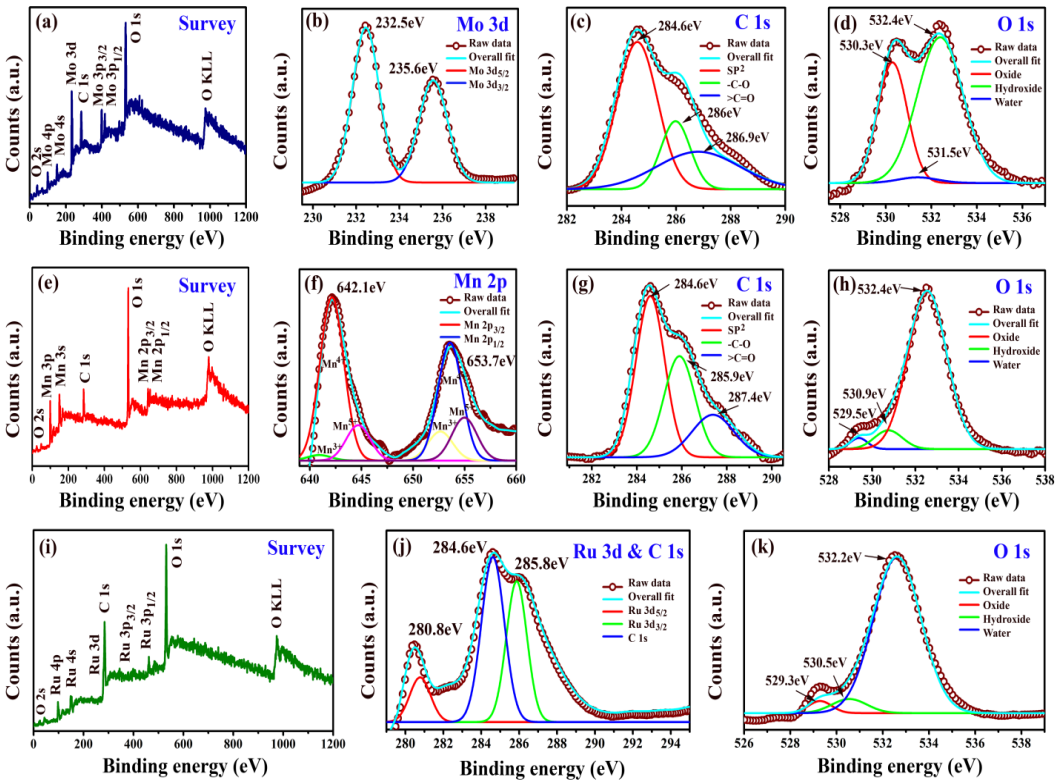

Figure 4.14. XPS spectra of MoO3/SWCNT composite: (a) survey spectrum, (b) Mo 3d, (c) C1s, (d) O1s; XPS spectra of MnO2/SWCNT composite: (e) survey spectrum, (d) Mn 2p,(c) C1s, (d) O1s: XPS spectra of RuO2/SWCNT composite: (i) survey spectrum, (j) Ru 3d, C1s and (d) O1s.

In Mn 2p spectrum multiple splitting with two main peaks can be identified at 642.1 and 653.7 eV corresponding to the excitation of Mn $2p_{3/2}$ and Mn $2p_{1/2}$ spin-orbit of Mn^{4+} in MnO_2, respectively (Figure 4.14f). The intensity of Mn^{3+} and Mn^{5+} related peaks is much weaker than that for Mn^{4+}, indicating the dominant role of Mn^{4+} in the composite.[7]The de-convoluted C 1s for MoO_3/SWCNT and MnO_2/SWCNT are shown in Figure 4.14c and Figure 4.14g respectively. The peak having binding energy 284.6 eV was assigned to the C=C bonds in CNT with SP^2 hybridization.[69] Furthermore, relatively small peaks at 286, 285.9 eV and 286.9 eV, 286.85 eV was assigned to the –C–O and >C = O functional group respectively.[70]Figure 4.14j shows the Ru 3d and C 1s spectra of the RuO_2/SWCNT nanocomposites. Two peaks of Ru 3d at 280.8 and 285.8 eV were assigned to Ru $3d_{5/2}$ and Ru $3d_{3/2}$ respectively, whereas the peak at 284.6 eV was assigned to the C=C bonds of C 1s.[3,71]The deconvoluted O 1s spectra as shown in the fig4.14(d), (h), (k) consist of three peaks at the binding energy of 530.3, 531.5 and

532.4 eV (for MoO_3/SWCNT), 529.5, 530.9 and 532.4 eV (for MnO_2/SWCNT) and 529.3, 530.5 and 532.2 eV (for RuO_2/SWCNT) corresponding to various oxygen-containing chemical bonds: oxide, hydroxide and water respectively.[72]

The specific surface area and porosity of the as-prepared nanocomposites have been investigated by N_2 adsorption and desorption measurements at 77 K. According to Brunauer-Emmett-Teller [BET] analysis, the total specific surface area of 151.4 m^2 /g, 122.8 m^2 /g, 142.6 m^2 /g were obtained for the MoO_3/SWCNT, MnO_2/SWCNT and RuO_2/SWCNT nanocomposites respectively (Figure 4.15c), which were much larger than that of the exfoliated metal oxides nanosheets (i.e. 55.7 m^2 /g, 48.6 m^2 /g, 53.5 m^2/ g for MoO_3, MnO_2 and RuO_2 nanosheets, Figure4.15a). The pore size distribution plots were obtained based on the adsorption data according to the Barrett-Joyner-Halenda (BJH) method. The D vs dV/dlogD plots for the exfoliated metal oxides (Figure 4.15b), TMOs/SWCNT composites (Figure 16d) indicates the existence of mesopores ranging from 2 to 5 nm within the nanocomposites. The total specific surface area (81.2 m^2 /g) and pore size distribution plots of the pristine SWCNT is shown in the figure 4.16(a) and (b) respectively. The large specific surface area and mesoporous structure can provide more active sites for electrochemical reactions, increase contact area and shortening ion diffusion paths between electrode and electrolyte, which are beneficial for electrolyte percolation and facilitate the ion diffusion.

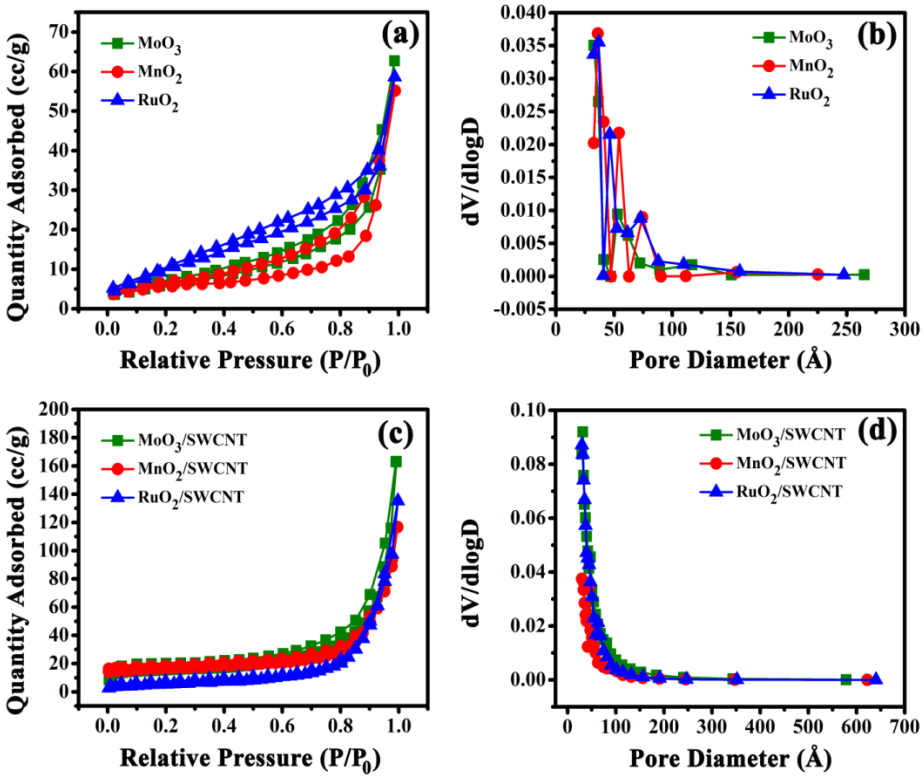

Fig. 4.15 (a,c) N_2 adsorption–desorption isotherms and (b,d) pore size distribution curves of the exfoliated MoO_3, MnO_2, RuO_2 nanosheets, and their composites with SWCNT respectively.

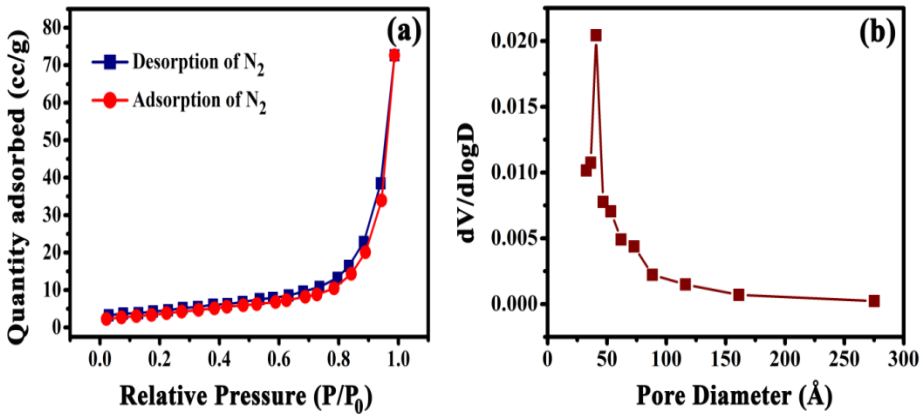

Figure4.16. Nitrogen adsorption-desorption isotherm (a)and corresponding pore size distribution curve (b) of the pristine SWCNTs.

4.5.3 Electrochemical study

4.5.3.1 Three electrodes measurement

We have systematically studied the electrochemical performance of the composite electrode materials both in two electrode and three electrode system. The as prepared thin films were transferred on gold coated PET for device fabrication. In the three electrode system we used Pt wire as a counter electrode, Ag/AgCl as a reference electrode and thin films on gold coated PET as a working electrode with 1 M Na_2SO_4 solution as a electrolyte. Cyclic voltammetry of the composite electrode materials were studied in the three electrode system (Figure 4.17) over the voltage window -1 to +1 V. The obtained specific capacitance values at 5 mv/s scan rate for the composite electrodes in three electrode systems are 1205.08F/g, 1168.69F/g and 1308.45F/g for MoO_3/SWCNT, MnO_2/SWCNT, and RuO_2/SWCNT electrodes respectively.

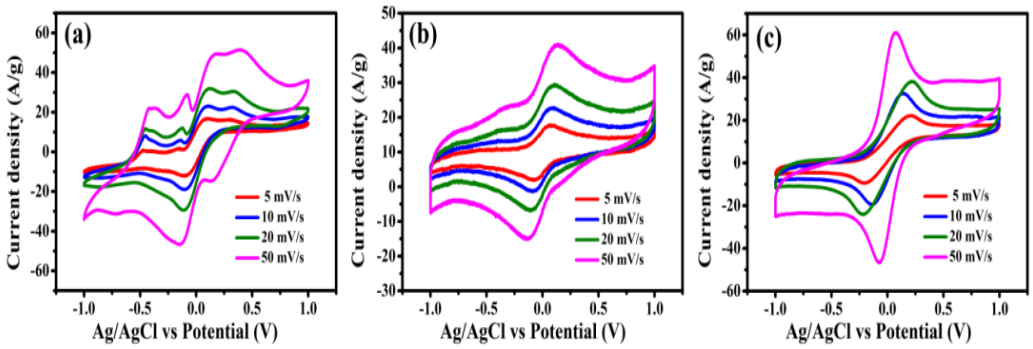

Figure.4.17 Cyclic voltammetry graph of (a) MoO_3/SWCNT,(b) MnO_2/SWCNT and (c) RuO_2/SWCNT at different scan rates respectively using three electrode system.

4.5.3.2 Two electrodes (Symmetric Solid State) Supercapacitor measurement

The symmetric solid state supercapacitors were prepared by these thin films with polyvinyl alcohol PVA-H_2SO_4 gel as a solid electrolyte sandwiched between the films. Cyclic voltammetry graph of the two electrode measurement for the composite electrode materials over the voltage window 0 V to +1 V shown in the Figure 4.18(a-c) at 5, 10, 20, 50, 100 mV/s scan rates. Galvanometric charging discharging performances of the two electrode system were also studied and are shown in the Figure 4.18(d-f). The maximum specific capacitance values at 5 mV/s scan rate are 717 F/g, 540 F/g, and 676 F/g for MoO_3/SWCNT, MnO_2/SWCNT and RuO_2/SWCNT electrodes respectively. Figure 4.18g shows that the specific capacitance decreases with scan rate for all three composites as expected.

The charge storage mechanism of the TMOs can be explained by following reversible redox reactions.

$$2MoO_3 + 2H^+ + 2e^- \leftrightarrow Mo_2O_5 \text{.....(3)}$$

$$MnO_2 + H^+ + e^- \leftrightarrow MnOOH \text{.....(4)}$$

$$RuO_2 + \beta H^+ + \beta e \leftrightarrow RuO_{2-\beta}(OH)\beta \text{.....(5)}$$

The stability of the symmetric supercapacitors was also tested through a cyclic voltammetry at a fixed scan rate of 100mV/s for 1000 cycles. The symmetric supercapacitor device made by MoO_3/SWCNT electrodes retained 91.99 % of its initial specific capacitance value after 1000 CV cycles, whereas for the MnO_2/SWCNT and RuO_2/SWCNT symmetric supercapacitor are 95.88 % and 92.25 % respectively which

indicative of excellent cycle stability of the symmetric supercapacitor devices as shown in the Figure 4.18h. The supercapacitor based on MoO_3/SWCNT composite electrode materials delivers a high energy density of 24.89Wh/Kg at a power density 1.61kW/kg. The RuO_2/SWCNT composite supercapacitor deliver energy density 23.48Wh/Kg at a power density 1.52kW/kg and that for MnO_2/SWCNT composite supercapacitor is 18.73Wh/Kg at a power density 1.21kW/kg. The Ragone plot of our devices and previously reported solid state supercapacitor devices is shown in the Figure 4.18(i). [73-78] We can see from the Ragone plot the performance of as prepared TMOs nanosheets/SWCNT composites are superior over previously reported metal oxide based supercapacitors in terms of specific capacitance and energy density.

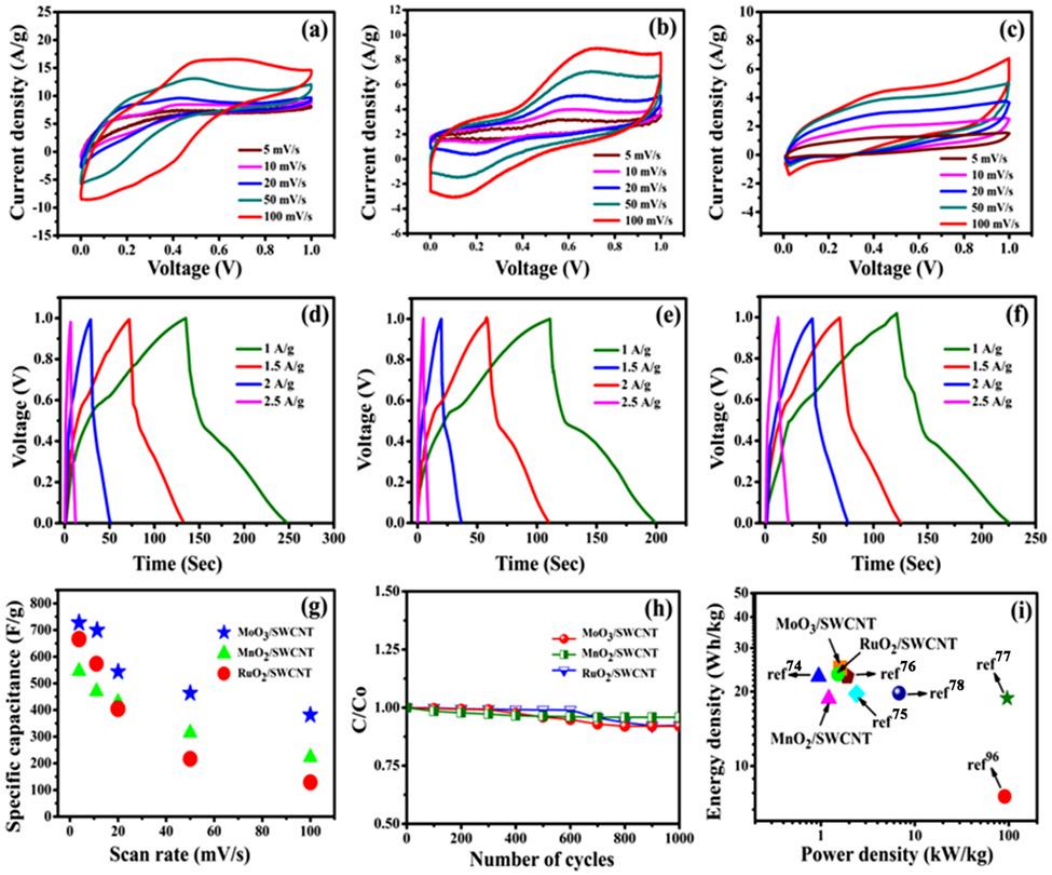

Figure. 4.18 Cyclic voltammetry graph of (a) MoO_3/SWCNT, (b) MnO_2/SWCNT and (c) RuO_2/SWCNT at different scan rates respectively; Galvanometric charging discharging graphs of (d) MoO_3/SWCNT, (e) MnO_2/SWCNT and (f) RuO_2/SWCNT at different current density respectively; (g) Scan rates vs specific capacitance graph of all TMOs/SWCNT composites; (h) C/C_o vs number of cycles graph of all TMOs/SWCNT;

(i) Ragone plot for TMOs/SWCNT composites solid-state supercapacitor devices, compared with other reported metal oxides.

We have also studied the electrochemical impedance spectroscopy of all the solid state supercapacitors. The upper inset of (Figure 4.19) represents the schematic equivalent circuit model of the system, where R_s is the equivalent series resistance, R_{ct} is the charge transfer resistance, Zw is the Warburg impedance, Cl is the electric double capacitance. The obtained equivalent series resistances (R_s) from the Nyquist plot (Figure 4.19) are 1.85 Ω, 2.73 Ω and 2.43 Ω for MoO_3/SWCNT, MnO_2/SWCNT and RuO_2/SWCNT electrodes respectively. The absence of semicircles in the high frequency region even in the zoomed image (lower inset of Figure 4.19) indicates low charge transfer resistance of the electrodes implying rapid charge transfer at electrode-electrolyte interfaces. The size of the semi-circle of Nyquist plot is not only depends on the pseudo capacitive reactions; it's also governed by the oxide-substrate interface resistance.[79]

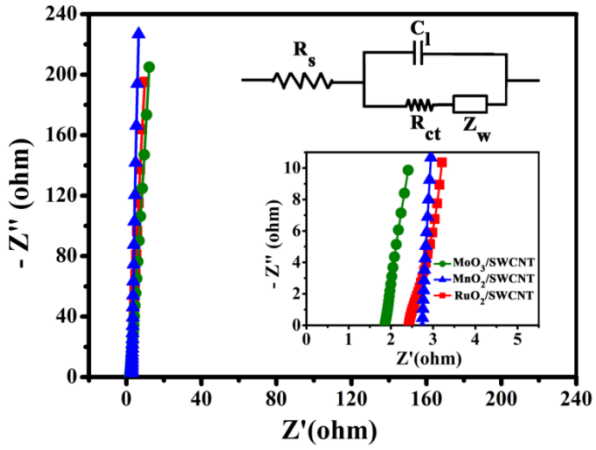

Figure 4.19. Nyquist plot of the all solid state supercapacitors; Inset showing the enlarge view of high frequency region and an equivalent circuit model.

Modern electronic devices are fast moving towards flexibility. To this end, we have investigated the behavior of our symmetric supercapacitors under a variety of bending conditions. The cyclic voltammetry of the solid state supercapacitors at different bending angle at 100 mV/s scan rate are shown in the Figure 4.20(a-c). The electrochemical performances of the device do not significantly change under various bending conditions. The specific capacitance values of the all the devices are almost remain same during bending, which is displayed in the Figure 4.20(d).

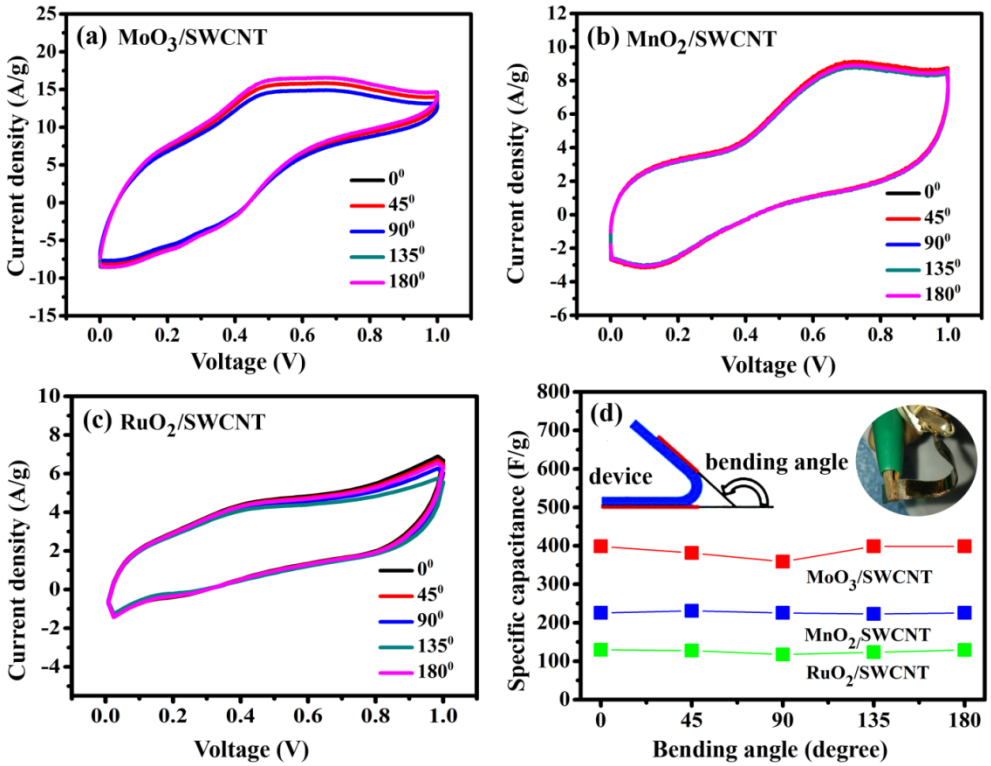

Figure.4.20 Cyclic voltammetry curves at different bending conditions at 100 mv/s scan rate for (a) MoO_3/SWCNT, (b) MnO_2/SWCNT and (c) RuO_2/SWCNT respectively.(d) Specific capacitance vs bending angle graph of all TMO/SWCNT composite.

4.5.3.1 Electrochemical study of In-plane Micro Supercapacitor based on MnO_2 and SWCNT

Fig.4.21 (a)-(f) shows the electrochemical performance of the as-fabricated in-plane supercapacitor based on MnO_2/SWCNT composite. Fig. 4.21(a) shows the cyclic voltrametry graph at different scan rates from 5mV/s to50 mV/s. The non-ideal rectangular shapes of the CV curves indicate the pseudo capacitive behaviors of the electrodes. The specific capacitances and areal capacitances of the in-plane supercapacitors were determined from the CV curves. The calculated areal capacitance values are 431.02 F/g, 365.85 F/g, 324.45 F/g,302.38 F/g, 290.15 F/g and 275 F/g at 5mv/s, 10 mV/s ,20 mV/s,30 mV/s,40 mV/s and 50 mV/s respectively. We have also calculated the corresponding areal capacitance values for different scan rates which are displays in the fig.4.21(c).Galvanometric charging discharging performances of the

planar-supercapacitors also studied at different current density shown in the fig.4.21 (b). The obtained maximum specific capacitance is 560.22 F/g (5.25mF/cm^2) at 1.65A/g current density As fabricated planar-supercapacitor shows excellent stability displays in the fig.18(d), with 97.4% of the maximum capacitance retained after 1000 cycles. The calculated energy density is 77.80 Wh/kg (2.62 mWh/cm^2) at a power density 3.50kW/kg (43.66mW/cm^2). We also performed electrochemical impedance spectroscopy tests to evaluate the capacitive performances of the micro-capacitors. The larger slope of the straight line at low frequency region in Nyquist plot in fig.4.21(e) implies better capacitive behavior with a series resistance of ~33 ohm. The excellent mechanical flexibility of the planar supercapacitors is demonstrated in the fig.4.21(f).The CV curves at different bending angels at 0°, 45°, 90°, 135°, and 180° were almost overlapped, elucidate the superior flexibility and electrochemical stability.

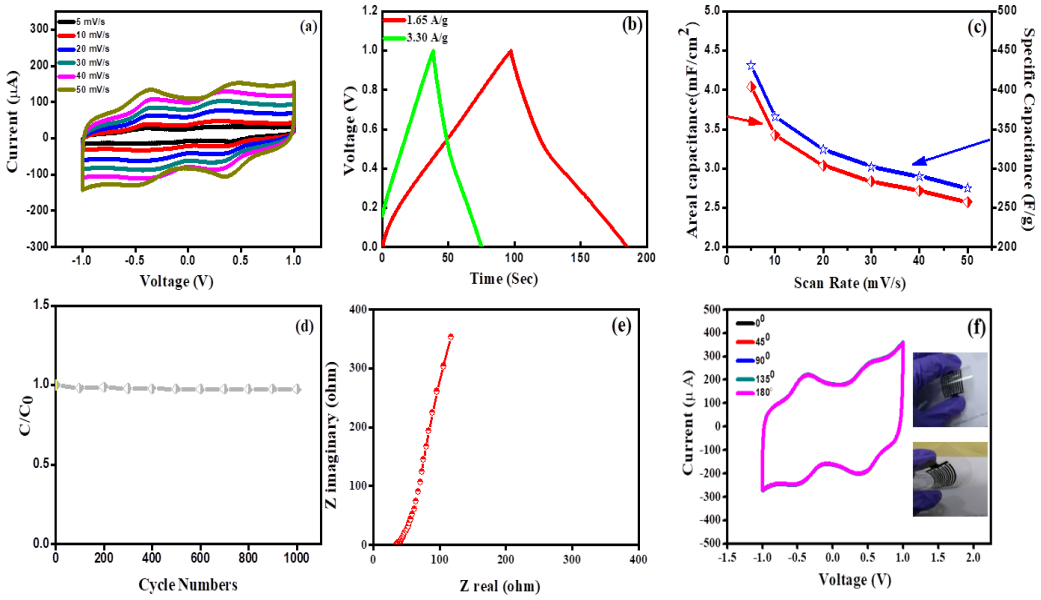

Figure 4.21. Cyclic voltammograms at different scan rates (a), Galvanostatic charge–discharge curves at different current density, (b) specific capacitance and areal cspacitance at different scan rates (c), Cycle stability graph (d), Nyquist plot(e), CV curves tested at 100 mV/s under different bending angels(f).

4.6 Summary

We have shown two poor solvents ethanol and water can be a good solvent for exfoliating TMOs when they combined in a particular volume fraction. This mixed solvent method is versatile, scalable and gives high concentration dispersion of TMOs nanosheets, higher than that reported previously. AFM and HRTEM study reveals that

the nanosheets are mostly bi-layer with average lateral size of 300 nm for MoO_3 and 200 nm for MnO_2 and RuO_2 respectively. Raman and XPS study shows this method gives dispersion of defect free nanosheets of TMOs. Composite thin film of TMOs nanosheets with SWCNT (25 wt%) deposited of gold coated PET exhibited ultra-high capacitance (1205.08 F/g for MoO_3-SWNT) in three electrode system with aqueous Na_2SO_4 as electrolyte. As fabricated thin film symmetric supercapacitors in all-solid-state based on TMOs nanosheets composites with SWCNT with polyvinyl alcohol PVA–H_2SO_4 gel as a solid electrolyte exhibit high specific capacitance (717 F/g, 540 F/g and 676 F/g for MoO_3-SWCNT, MnO_2-SWCNT and RuO_2-SWCNT respectively), excellent flexibility and long cycle life, leading to an extremely high energy density (24.89 Wh/Kg at 1.61 kW/kg, 18.73 Wh/Kg at 1.21 kW/Kg and 23.48 Wh/Kg at 1.52 kW/Kg), whereas, in-plane micro supercapacitors based on few layered MnO_2 and SWCNT hybrid displayed excellent specific capacitance of 560.22 F/g with significant energy density of 77.80 Wh/kg and excellent cycling stability even after 1000 cycles. Our findings represent a promising direction and significant steps towards exfoliating TMOs to produce 2D oxide nanosheets in low toxic mixed solvent for flexible energy storage device with high energy density.

4.7. References

1. W. Tang, L. Liu, S. Tian, L. Li, Y. Yue, Y. Wu and K. Zhu, *Chem. Commun.,* 2011, **47**,10058-10060.
2. F. Luan, G. Wang, Y. Ling, X. Lu, H. Wang, Y. Tong, X.X. Liu and Y. Li, *Nanoscale*, 2013, **5**, 7984-7990.
3. L.K. Naslund, A. S. Ingason, S. Holmin and J. Rosen, *J. Phys. Chem. C*, 2014**, 28**, 15315-15323.
4. X. Lu, G. Wang, T. Zhai, M. Yu, J. Gan, Y. Tong and Y. Li, *Nano Lett.*, 2012, **12**, 1690-1696.
5. X. Lu, T. Zhai, X. Zhang, Y. Shen, L. Yuan, B. Hu, L. Gong, J. Chen, Y. Gao, J. Zhou, Y.Tong and Z. L. Wang, *Adv. Mater*.**,** 2012, **24**, 938-944.
6. G. Yu, L. Hu, N. Liu, H. Wang, M. Vosgueritchian, Y. Yang, Y. Cui and Z. Bao, *Nano Lett.*, 2011, **11**, 4438-4442.
7. Y. Zhao, Y. Meng, H. Wu, Y. Wang, Z. Wei, X. Li and P. Jiang, *RSC Adv.*, 2015, **5**, 90307-90312.

8. L. Wu, R. Li, J. Guo, C. Zhou, W. Zhang, C. Wang, Y. Huang, Y. Li and J. Liu, *AIP Adv.*, 2013, **3**, 082129.
9. L. Peng, X. Peng, B. Liu, C. Wu, Y. Xie and G. Yu, *Nano Lett.*, 2013, **13**, 2151-2157.
10. J. Feng, X. Sun, C. Wu, L. Peng, C. Lin, S. Hu, J. Yang and Y. Xie, *J. Am. Chem. Soc.*, 2011, **133**, 17832-17838.
11. J. Xie, X. Sun, N. Zhang, K. Xu, M. Zhou and Y. Xie, *Nano Energy*, 2013, **2**, 65-74.
12. J. Yan, Z. Fan, W. Sun, G. Ning, T. Wei, Q. Zhang, R. Zhang, L. Zhi and F. Wei, *Adv. Funct.Mater.*, 2012, **22**, 2632-2641.
13. V. Gupta, T. Kusahara, H. Toyama, S. Gupta and N. Miura, *Electrochem. Commun*., 2007, **9**, 2315-2319.
14. H. Wang, Q. Hao, X. Yang, L. Lu and X. Wang, *Nanoscale*, 2010, **2**, 2164-2170.
15. K. Jurewicz, S. Delpeux, V. Bertagna, F. Beguin and E. Frackowiak, *Chem. Phys. Lett*., 2001, **347**, 36-40.
16. J. Tao, N. Liu, W. Ma, L. Ding, L. Li, J. Su and Y. Gao, *Sci. Rep.*, 2013, **3**, 2286.
17. A. Laforgue, P. Simon, C. Sarrazin and J.F. Fauvarque, *J. Power Sources*. 1999, **80**, 142-148.
18. L. Pan, G. Yu, D. Zhai, H. R. Lee, W. Zhao, N. Liu, H. Wang, B. C. K. Tee, Y. Shi, Y. Cui and Z. Bao, *Proc. Natl. Acad. Sci. U. S. A.*, 2012, **109**, 9287-9292.
19. J. J. Yoo, K. Balakrishnan, J. Huang, V. Meunier, B. G. Sumpter, A. Srivastava, M. Conway, A. L. M. Reddy, J. Yu, R. Vajtai and P. M. Ajayan, *Nano Lett.*, 2011**, 11**, 1423-1427.
20. X. Huang, X. Qi, F. Boey and H. Zhang, *Chem. Soc. Rev.*, 2012, **41**, 666-686.
21. A. K. Geim and K. S. Novoselov, *Nat. Mater.*, 2007, **6**, 183-191.
22. X. Huang, C.Tan, Z. Yin and H. Zhang, *Adv. Mater.*, 2014, **26**, 2185-2204.
23. F. Bonaccorso, L. Colombo, G. Yu, M. Stoller, V. Tozzini, A. C. Ferrari, R. S. Ruoff and V. Pellegrini, *Science*, 2015, **41**, 347.
24. S. Dutta, S. Pal and S. De, *New J. Chem.*, 2018, **42**, 10161-10166.
25. G. Wang, X.G. Zhu, Y.Y. Sun, Y.Y. Li, T. Zhang, J. Wen, X.Chen, K. He, L.L. Wang, X.C. Ma, J.F. Jia, S. B. Zhang and Q.K. Xue, *Adv. Mater.*, 2011, **23**, 2929-2932.
26. C. Y. Zhi, Y. Bando, C. C. Tang, H. Kuwahara and D. Golberg, *Adv. Mater.*, 2009, **21**, 2889-2893.

27. B. Radisavljevic, A. Radenovic, J. Brivio, V. Giacometti and A. Kis, *Nat. Nanotechnol.*, 2011, **6**, 147-150.
28. W. J. Yu, S. Y. Lee, S. H. Chae, D. Perello, G. H. Han, M. Yun and Y. H. Lee, *Nano Lett.*, 2011, **11**, 1344-1350.
29. S. Yin, Y. Zhang, J. Kong, C. Zou, C. M. Li, X. Lu, J. Ma, F. Y. C. Boey and X. Chen, *ACS Nano*, 2011, **5**, 3831-3838.
30. K. Chang and W. Chen, *ACS Nano*, 2011, **5**, 4720-4728.
31. J. Jiang, Y. Li , J. Liu , X. Huang , C. Yuan and X. W. Lou, *Adv. Mater.*, 2012, **24**, 5166-5180.
32. C. C. Hu, W. C. Chen and K. H. Chang, *J. Electrochem. Soc.*, 2004, **151**, A281-A290.
33. Y. T. Kim, K. Tadai and T. Mitani , *J. Mater. Chem.*, 2005, **1**, 4914-4921.
34. L. Peng, P. Xiong, L. Ma, Y. Yuan, Y. Zhu, D. Chen, X. Luo, J. Lu, K. Amine and G. Yu, *Nat.Commun.*, 2017, **8**, 15139.
35. R.J. Smith, P.J. King, M. Lotya, C. Wirtz, U. Khan, S. De, A. O'Neill, G.S. Duesberg, J.C. Grunlan, G. Moriarty, J. Chen, J. Wang, A. Minett, V. Nicolosi and J.N. Coleman, *Adv. Mater.*,2011, **23**, 3944-3948.
36. J.N. Coleman, M. Lotya, A.O' Neill, S.D. Bergin, P.J. King, U. Khan, K. Young, A. Gaucher and S. De, *Science*, 2011, **331**, 568-571.
37. M. Lotya, P.J. King, U. Khan, S. De and J.N. Coleman, *ACS Nano*, 2010, **4**, 3155-3162.
38. U. Khan, A.O' Neill, M. Lotya, S. De and J. N Coleman, *Small*, 2010, **6**, 864-871.
39. M. Lotya, Y. Hernandez, P.J. King, R.J. Smith, V. Nicolosi, L.S. Karlsson, F.M. Blighe and S.De, *J. Am. Chem. Soc.*, 2009, **131**, 3611-3620.
40. Y. Hernandez, V. Nicolosi, M. Lotya, F. M. Blighe, Z. Sun, S. De, I. T. McGovern, B. Holland, M. Byrne, Y. K. Gun'Ko, J. J. Boland, P. Niraj, G. Duesberg, S. Krishnamurthy, R. Goodhue, J. Hutchison, V. Scardaci, A. C. Ferrari and J. N. Coleman, *Nat. Nanotech.*, 2008, **3**, 563–568.
41. D. Hanlon, C. Backes, T. M. Higgins, M. Hughes, A. O'Neill, P. King, N. McEvoy, G. S. Duesberg, B. M. Sanchez, H. Pettersson, V. Nicolosi and J. N. Coleman, *Chem. Mater.*, 2014, **26**, 1751–1763.

42. P. Blake, P. D. Brimicombe, R. R. Nair, T. J. Booth, D. Jiang, F. Schedin, L. A. Ponomarenko, S. V. Morozov, H. F. Gleeson, E. W. Hill, A. K. Geim and K. S. Novoselov, *Nano Lett.*, 2008, **8**, 1704-1708.
43. X. Cui, C. Z.Zhang, R. Hao and Y. L. Hou, *Nanoscale*, 2011, **3**, 2118-2126.
44. G. Cunningham, M.Lotya, C.S. Cucinotta, S.Sanvito and S. D. Bergin, *ACS Nano*, 2012, **6**, 3468-3480.
45. K.G. Zhou, N.N. Mao, H.X. Wang, Y. Peng and H.L. Zhang, *Angew. Chem. Int. Ed.*, 2011, **50**, 10839-10842.
46. A. A. Green and M. C. Hersam, *Nano Lett.*, 2009, **9**, 4031-4036.
47. A. B. Bourlinos, V. Georgakilas and R. Zboril, *Solid State Commun.*, 2009, **149**, 2172-2176.
48. P. May, U. Khan, J.M. Hughes and J. N. Coleman, *J. Phys. Chem. C.*, 2012, **116**, 11393-11400.
49. A. O'Neill, U. Khan, P. N. Nirmalraj, J. Boland and J. N. Coleman, *J. Phys. Chem. C*, 2011, **115**, 5422-5428.
50. C. M. Hansen, *CRC, Boca Raton*, 2007**.**
51. J. N. Coleman, *Adv. Funct. Mater.* 2009, **19**, 3680-3695.
52. K. Kai, Y. Yoshida, H. Kageyama, G. Saito, T. Ishigaki, Y. Furukawa and J. Kawamata, *J. Am. Chem. Soc*., 2008, **130**, 15938-15943.
53. K. Kalantar-zadeh, J. Tang, M. Wang, K. L. Wang, A. Shailos, K. Galatsis, R.Kojima, V. Strong, A. Lech, W. Wlodarski and R. B. Kaner, *Nanoscale*, 2010, **2**, 429-433.
54. M. Osada and T. Sasaki, *J. Mater. Chem.*, 2009, **19**, 2503-2511.
55. S.J. Choi, J.S. Jang, H. J.Park and I.D. Kim, *Adv. Funct. Mater.*, 2017, 1606026.
56. Y. Wang, Y. Zhu, Z.Xing and Y.Qian, *Int. J. Electrochem. Sci.*, 2013, **8**, 9851-9857.
57. Y. Chen, C. Lu, L. Xu, Y. Ma, W. Hou and J.J. Zhu, *CrystEngComm.*, 2010, **12**, 3740-3747.
58. X. Zhang, P. Yu, H. Zhang, D. Zhang, X. Sun and Y. Ma, *Electrochim. Acta*, 2013, **89**, 523-529.
59. J. Zhou, L. Yu, M. Sun, S. Yang, F. Ye, J. He and Z. Hao, *Ind. Eng. Chem. Res.*, 2013, **52**, 9586-9593.
60. J. Liu, J. Jiang, C. Cheng, H. Li, J. Zhang, H. Gong and H. J. Fan, *Adv. Mater.*, 2011, **23**, 2076-2081.

61. N. Soin, S.S. Roy, C.O Kane, T.H. Lim, C.J.D. Hetherington and J.A. McLaughlin, *CrystEngComm.,* 2011, **13**, 312-318.
62. N. Soin, S. S. Roy, T. H. Lim and J. A. D. McLaughlin, *J. Mater. Chem.,* 2011, **129**, 1051-1057.
63. J.X. Wang, S.R. Brankovic, Y. Zhu, J.C. Hanson and R.R. Adzi, *J. Electrochem. Soc.,* 2003, **150**, A1108-A1117.
64. T. Siciliano, A. Tepore, E. Filippo, G. Micocci and M. Tepore, *Mater. Chem. Phys.,* 2009, **114**, 687.
65. A. Ogata, S. Komaba, R. Baddour-Hadjean, J.P. Pereira-Ramos and N. Kumagai, *Electrochim Acta,* 2008, **53**, 3084-3093.
66. S. Y. Mar, C. S. Chen, Y. S. Huang and K. K. Tiong, *Appl. Surf. Sci.,* 1995, **90**, 497-504.
67. B. Mendoza-Sánchez and P. S. Grant,. *Electrochim. Acta,* 2013, **98**, 294-302.
68. Y.C. Lin, W. Zhang, J.K. Huang, K.K. Liu, Y.H. Lee, C.T. Liang, C.W. Chu and L.J. Li, *Nanoscale,* 2012, **4**, 6637-6641.
69. R. S. Kalubarme, Y.H. Kim and C.J. Park, *Nanotechnology*, 2013, **24**, 365401.
70. B. Wu, C. Wang, Y. Cui, L. Mao and S. Xiong, *RSC Adv.,* 2015, **5**, 16986-16992.
71. J.C. Chou, Y.L. Chen, M.H. Yang, Y.Z. Chen, C.C. Lai, H.T. Chiu, C.Y. Lee, Y.L. Chueh and J.Y. Gan, *J. Mater. Chem. A,* 2013, **1**, 8753-8758.
72. H. Xia, M. Lai and L. Lu, *J. Mater. Chem.,* 2010, **20**, 6896-6902.
73. Y. Shao, H. Wang, Q. Zhang and Y. Li, *J. Mater. Chem. C,* 2013, **1**, 1245-1251.
74. J. Yang, G. Li, Z. Pan, M. Liu, Y. Hou, Y. Xu, H. Deng, L. Sheng, X. Zhao, Y. Qiu and Y.Zhang, *ACS Appl. Mater. Interfaces*, 2015, **7**, 22172-22180.
75. H. Su, P. Zhu, L. Zhang, F. Zhou, G. Li, T. Li, Q. Wang, R. Sun and C. Wong, *J. Electroanal. Chem.,* 2017, **786**, 28-34.
76. P.C. Chen, H.T. Chen, J. Qiu and C.W. Zhou, *Nano Res.*, 2010, **3**, 594-603.
77. B.G. Choi, S.J Chang, H.W. Kang, C.P. Park, H.J. Kim, W.H. Hong, S. Lee and Y.S. Huh, *Nanoscale,* 2012, **4**, 4983-4988.
78. J. Duay, E. Gillette, R. Liu and S.B. Lee, *Phys. Chem.*, 2012, **14**, 3329-3337.
79. A. Allison and H.A. Andreas, *J. Power Sources.*, 2019, **426**, 93–96.